Heliyon 9 (2023) e20125

Contents lists available at ScienceDirect

Heliyon

journal homepage: www.cell.com/heliyon

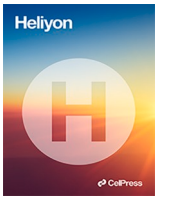

Exploring ozone formation rules and concentration response to the change of precursors based on artificial neural network simulation in a typical industrial park

Qiaoli Wang [a,*], Dongping Sheng [a], Chengzhi Wu [c], Jingkai Zhao [a], Feili Li [a], Shengdong Yao [a], Xiaojie Ou [a], Wei Li [b], Jianmeng Chen [a,d,**]

[a] College of Environment, Zhejiang University of Technology, Hangzhou, 310032, China
[b] Key Laboratory of Biomass Chemical Engineering of the Ministry of Education, Institute of Industrial Ecology and Environment, College of Chemical and Biological Engineering, Zhejiang University (Zijingang Campus), Hangzhou, 310030, China
[c] Trinity Consultants, Inc. (China Office), Hangzhou, 310012, China
[d] Zhejiang University of Science & Technology, Hangzhou, 310023, China

ARTICLE INFO

Keywords:
Ozone formation rules
Sensitivity and response analysis
Maximum incremental reactivity
Artificial neural network

ABSTRACT

Industrial parks have more complex O_3 formation mechanisms due to a higher concentration and more dense emission of precursors. This study establishes an artificial neural network (ANN) model with good performance by expanding the moment and concentration changes of pollutants into general variables of meteorological factors and concentrations of pollutants. Finally, the O_3 formation rules and concentration response to the changes of volatile organic compounds (VOCs) and nitrogen oxides (NOx) was explored. The results showed that the studied area belonged to the NOx-sensitive regime and the sensitivity was strongly affected by relative humidity (RH) and pressure (P). The concentration of O_3 tends to decrease with a higher P, lower temperature (Temp), and medium to low RH when nitric oxide (NO) is added. Conversely, at medium P, high Temp, and high RH, the addition of nitrogen dioxide (NO_2) leads to a larger decrease capacity in O_3 concentration. More importantly, there is a local reachable maximum incremental reactivity (MIR_L) at each certain VOCs concentration level which linearly increased with VOCs. The general maximum incremental reactivity (MIR) may lead to a significant overestimation of the attainable O_3 concentration in NOx-sensitive regimes. The results can significantly support the local management strategies for O_3 and the precursors control.

1. Introduction

The implementation of strong policies and harsh measures has significantly improved the total ambient air quality in China. However, ambient ozone (O_3) pollution is still increasingly severer [1,2], exerting significant impacts on human health and the atmospheric environment [3]. It is generally recognized that volatile organic compounds (VOCs) and nitrogen oxides (NO_X) are the two dominant precursors [4]. However, the secondary photochemical conversion of VOCs and NO_X are nonlinear and influenced by several spatial-temporal heterogeneity factors [1,5], as well as complex affection from meteorological factors [6,7]. Consequently, the

* Corresponding author.
** Corresponding author. College of Environment, Zhejiang University of Technology, Hangzhou, 310032, China.
E-mail addresses: wangqiaoli@zjut.edu.cn (Q. Wang), jchen@zjut.edu.cn (J. Chen).

https://doi.org/10.1016/j.heliyon.2023.e20125
Received 28 August 2023; Received in revised form 12 September 2023; Accepted 12 September 2023
Available online 14 September 2023

underlying mechanisms governing O_3 pollution remain unclear. Therefore, in recent years, the focus has shifted from particle control to cooperative control for air quality improvement. Moreover, the efficient cooperative control of the pollution of VOCs, NO_X, and O_3 is an important challenge to serve "ecological civilization construction" and achieve a "beautiful China".

Meanwhile, the State Council requires governments at all levels to promote the action of *withdrawing from the city and entering the park*, resulting in enhanced production concentration within these parks alongside intensified pollutant emissions [8–11]. The atmospheric condition in industrial parks is different with that in relatively low polluted areas, due to the characterization of small-scale, dense enterprises and various chemical and complex production processes [12–14], as well as the intermittent and fugitive emissions of VOCs [15,16] and the inevitable emissions of NO_X [17,18], resulting in more complex in O_3 formation rules [19].

Previously, many studies have been carried out to explore the mechanism of O_3 photochemical conversion, particularly focusing on the ozone formation potential (OFP) and Empirical Kinetic Modeling Approach (EKMA) curve theory, which are widely applied in macro control of O_3 precursors [20]. Additionally, the observation-based model (OBM) utilized relative incremental reactivity (RIR) to simulate the O_3 response to the change of individual precursors [21]. Many interesting phenomena were found. Reducing anthropogenic VOCs is the most efficient way to mitigate O_3 pollution; additionally, the missing peroxy radical source will further extend NOx-limited conditions to the earlier time in a day [22,23]. With a comprehensive 1-D model of the Master Chemical Mechanism (MCM), the photolysis of the oxygenated volatile organic compounds (OVOC) was found to be the largest free-radical source in the boundary layer [19]. However, the macro control mechanisms encounter challenges in supporting atmospheric pollution prevention in industrial parks, as the application of the maximum incremental reactivity (MIR) theory may lead to an overestimation of O_3 pollution since the atmospheric conditions are mostly not the best for O_3 incremental reactivity. Keding Lu [24] reviewed that the chemistry for high VOCs and low NOx conditions are still insufficient. Hence, the actual atmospheric environmental conditions should be considered for studying O_3 formation rules and a quick response of control strategies to O_3 pollution in industrial parks [25]. Therefore, the impact of precursors on the O_3 formation process and the sensitive response of the precursors concentration change to O_3 formation in industry parks with high pollutant concentrations are still eager to discover.

Machine learning, which has the advantages of fast convergence speed, strong adaptability of prediction fragments, high precision, and low cost, is increasingly applied for processing large amounts of atmospheric monitoring data [26–28]. Deep learning networks, random forest (RF), support vector machines, and ensemble approaches have shown high performance, especially for air quality and PM concentration prediction [29–34]. Input variables, are one of the key problems in machine learning, directly affecting the complexity and generalization ability of prediction models. The conventional meteorological parameters and air pollution monitoring species are generally used for O_3 concentration prediction. Furthermore, some studies added other relative variables such as OFP, dew point, and direct solar radiation time, with algorithms like RF, minimum optimization variables, and recurrent neural network (RNN) to predict O_3 concentration [35,36]. However, other important information, such as sunlight and industrial production intensities, is still excluded. The moment carries some information related to diurnal-varied factors related to sunlight and industrial production intensity to a certain extent. Additionally, the pollutant concentration variation carries the information in the change of time series, especially in the record of the sudden exhaust from industrial sources [30].

In this study, one-year monitoring data of meteorological parameters and pollutants, in 2018, in a typical chemical industrial park were applied. The variables of the moment and concentration changes of pollutants were added to build an expanded dataset. An optimized Artificial Neural Network (ANN) model was built to explore the mechanism by controlling variables and interpolating target variables within the simulation space. Furthermore, O_3 formation rules and its response to the concentration change of VOCs and NOx were explored individually. The results strongly support the rapid, comprehensive, and accurate control of air pollution in industrial parks.

2. Methods

2.1. Datasets

The ZhaPu chemical industrial park (ZP Park) is a provincial-level economic development zone, which located in the southern Yangtze River Delta with four distinct seasons. ZP Park is dominated by bulk chemical materials, metal products, warehousing, and logistics with sound industry chain and large industrial scale, selected as the top 10 chemical parks in China. The park exhibits a typical industrial pollution characteristic due to the presence of densely distributed industrial emission sources and their high intensity emissions. Therefore, this park suffers from O_3 pollution due to the high VOCs and NO_X concentration by industrial and transportation emissions.

In 2018, continuous automatic monitoring data of meteorological parameters and pollutants were collected from the monitoring site. The monitoring data was extracted from the Automatic Ambient Air Monitoring Site located in ZP Park, which serves as a local atmospheric management facility. The testing equipment is subject to routine maintenance and monitoring in accordance with national guidelines. The meteorological parameters included temperature (Temp), pressure (P), relative humidity (RH), wind speed (WS), and wind direction (WD), monitored by the WS500-UMB weather system. As to the pollutants, VOCs were monitored by gas chromatography−mass spectrometry with flame ionization detection, 70 species was monitored with the detecting limit of 0.15 ppb [37]; nitric oxide (NO) and nitrogen dioxide (NO_2) were monitored by NO–NO_2-NO_X gas chemiluminescence analyzer method limited by 0.4 ppb; $PM_{2.5}$ was monitored by β-ray particle concentration tester applying gas filter correlation analysis method with the detecting limit of 0.004 mg m^{-3}; CO was monitored by CO gas analyzer limited by 0.04 ppm, and O_3 was monitored by ultraviolet absorption spectrophotometry limited by 0.05 ppb. $PM_{2.5}$ was included since most studies have explicitly pointed out its negative correlation to O_3. CO was also discovered to participate in atmospheric oxidation-reduction reactions. The moment of 0–23 was also

compiled as a feature for the extension of the initial dataset. Furthermore, all concentration changes of pollutants, also as the extension, were calculated by the concentration difference at the next and the current hour, as shown in Eq. (1).

$$\Delta C_{i,t} = C_{i,t+1} - C_{i,t} \tag{1}$$

where $C_{i,t+1}$ and $C_{i,t}$ refer to the concentrations of pollutant i at moments $t+1$ and t, respectively. $\Delta C_{i,t}$ refers to the concentration change of pollutant i at the moment t.

Thus, an expanded dataset D_e was compiled in Eq. (2) as follows:

$$D_e = \{(\boldsymbol{x}_n, y_n)\}, \boldsymbol{x}_n = (x_{n1}, x_{n2}, \cdots, x_{nd}) \tag{2}$$

where, $\boldsymbol{x}_n$ refers to a d-dimensional vector containing variables of the moment, Temp, P, RH, WS, WD, concentrations, and the change of concentrations of VOCs, NO, NO_2, $PM_{2.5}$, and CO. $d = 16$ in this study. n refers to the 8651 samples in this study. y_n refers to the corresponding value of O_3 concentration.

Simultaneously, the general dataset D_g was also compiled with the variables of concentrations of VOCs, NO, NO_2, $PM_{2.5}$, CO, and meteorological parameters of Temp, P, RH, WS, and WD in Eq. (3) as follows:

$$D_g = \left\{\left(\boldsymbol{x}_n^{'}, y_n\right)\right\}, \boldsymbol{x}_n^{'} = (x_{n1}, x_{n2}, \cdots, x_{nl}) \tag{3}$$

where, $\boldsymbol{x}_n^{'}$ refers to an l-dimensional vector containing the variables of Temp, P, RH, WS, WD, and concentrations of VOCs, NO, NO_2, $PM_{2.5}$, and CO. $l = 10$ in this study.

2.2. ANN model

The ANN model is particularly well suited to dealing with nonlinear problems [38,39]. It is an extensive, parallel, interconnected network composed of simple adaptive units whose organization can simulate the interaction of the biological nervous system in the real world. In the past ten years, ANN has made significant progress and solved many practical problems, including pattern recognition, intelligent robot, automatic control, and forecast estimates. In this study, Bayesian regularization back propagation was applied for training, which updates the weight and bias values according to Levenberg-Marquardt optimization. Additionally, it modifies the linear combination of squared errors and weights to enhance generalization capabilities.

The training was executed by dividing the expanded and general datasets D_e and D_g, respectively, into three parts of 0.7 training set, 0.15 test set, and 0.15 validation set. The 3-layer networks of $\boldsymbol{x}_n$ and $\boldsymbol{x}_n^{'}$ served as the input layer and y_n served as the output layer. After optimizing the parameters, the number of neural units in the hidden layer was adjusted. The simulation performances [3,18] of the finally optimized ANNs were evaluated by R-square (R^2), mean squared error (MSE), mean absolute error (MAE), and the sum of squares due to error (SSE), as shown in Eqs. (4)–(7). A good simulation performance implies that R^2 and the rest evaluation parameters are close to 1 and 0, respectively.

$$R^2 = 1 - \frac{\sum_{j=1}^{n}\left(O_j - S_j\right)^2}{\sum_{j=1}^{n}\left(O_j - \overline{O}\right)^2} \tag{4}$$

$$MSE = \frac{1}{n}\sum_{j=1}^{n}\left(O_j - S_j\right)^2 \tag{5}$$

$$MAE = \frac{\sum_{j=1}^{n}\left|O_j - S_j\right|}{n} \tag{6}$$

$$SSE = \sum_{j=1}^{n}\left(O_j - S_j\right)^2 \tag{7}$$

where, O_j and S_j refer to the observed and simulated concentrations of O_3, respectively. $\overline{O}$ refers to the average observed concentration of O_3.

2.3. Reactivity and sensitive analysis

Incremental reactivity (IR) is used for investigating the influence of the change of the concentrations of VOCs and NOx on O_3 formation [40]. The IR of O_3 concentration for unit concentration changes of NO_X and VOCs were calculated to normalize the increments of the concentrations of VOCs and NO_X, according to Eq. (8) and **(9)**.

$$IR_{NO_x} = \frac{\Delta C_{O_3,t}}{\Delta C_{NO_x,t}} \tag{8}$$

$$IR_{VOCs} = \frac{\Delta C_{O_3,t}}{\Delta C_{VOCs,t}} \tag{9}$$

where IR_{NOx} and IR_{VOCs} refer to the IR of O_3 concentration for unit concentration changes of NO_X and VOCs, respectively.

3. Results and discussion

3.1. Distribution characteristics of variables

Due to the complicated rules of O_3 formation, there is significant uncertainty in the prediction of the conditions that are out of the feature space but are of high performance within the prediction fragment. Meanwhile, the samples collected from the local monitoring site contained the most locally occurring conditions. Therefore, initially, a comprehensive distribution analysis was conducted to determine the feature boundary for exploring the O_3 formation rules within an appropriate simulation space with high accuracy.

The simulation data characterization was systematically analyzed through various forms of visualization. As shown in Fig. 1(a), the distributions for Temp, RH, and P ranged from −4.30 °C – 36.25 °C, 21.77%–100%, and 98.51 kPa–103.49 kPa, respectively, with the most frequent values of 28.14 °C, 100%, and 101.845 kPa. Additionally, considering a particular RH condition of 100%, another peak of 85.92% was applied as another frequent condition in this study. Additionally, the dominant WD and average WS were east and 2.83 m s^{-1}, respectively, as shown in Fig. 1(b). As shown in Fig. 1(c), a relatively strong negative correlation of −0.86 was identified between Temp and P. Additionally, the distributions of Temp, P, and RH were color-coded based on O_3 concentration levels. The analysis revealed higher concentrations of O_3 occurred more frequently at elevated Temp, lower P, and moderate to low RH.

For atmospheric pollutants, as shown in Fig. 2(a). The probability density distributions of VOCs and NO exhibit a high frequency at

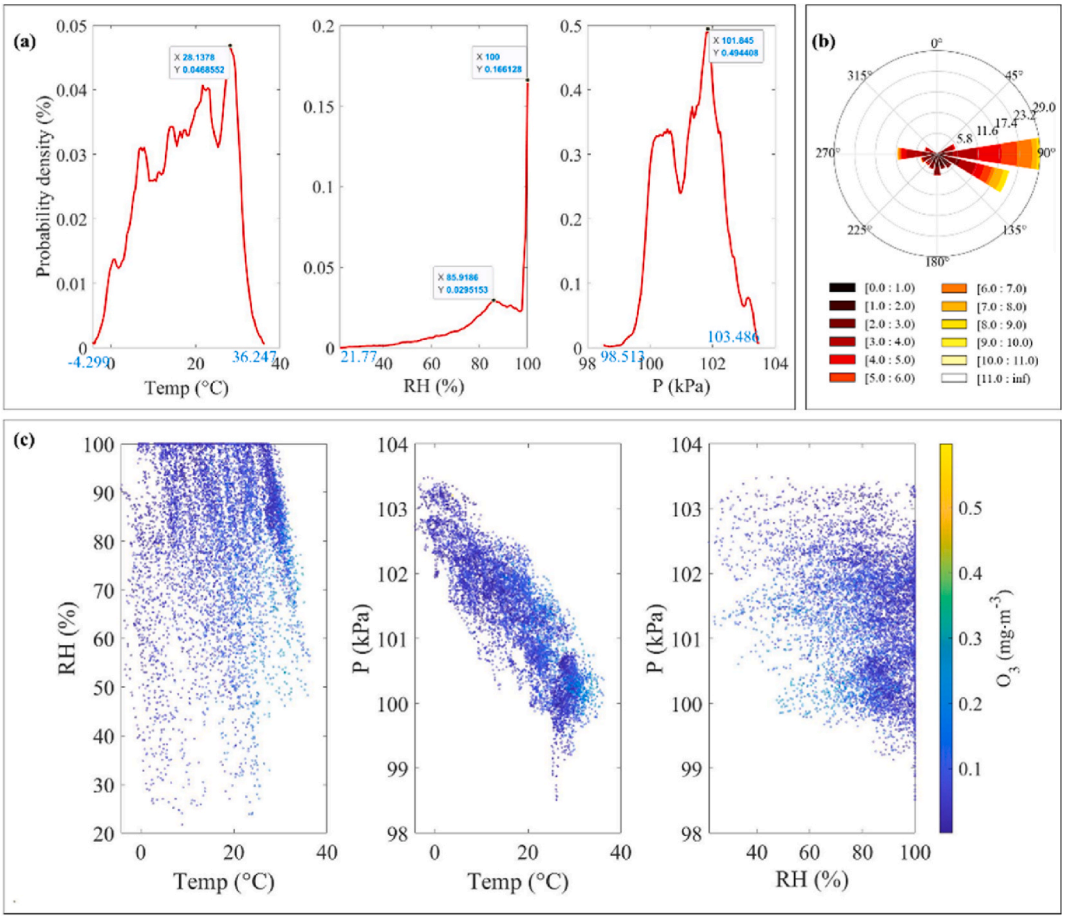

Fig. 1. The distribution of meteorological parameters. (a) The distributions of probability density for Temp, RH, and P; (b) Windrose of WS and WD; (c) Scatter distributions among Temp, P and RH to O_3 concentration.

low concentrations with a long-range tail, indicating that the general concentrations of VOCs and NO are not high. However, instantaneous spikes in concentration may occur due to industrial emissions. The most frequent concentrations occurred at 0.0117, 0.0547, 0.0203, and 0.595 mg m^{-3} of NO_2, O_3, $PM_{2.5}$, and CO, respectively.

Additionally, the distributions were analyzed in pairs. The general distributions of VOCs to NO, NO_2, and NO_X revealed a typical "*L*" style with dominant distribution in two areas: low VOCs with a large range of NO_X and low NO_X with a large range of VOCs. The concentrations of VOCs were handled by natural logarithm operation for better visuality, as shown in Fig. 2(b) a relatively high O_3 concentration most frequently occurred at the atmospheric condition of low NO_X with a large range of VOCs. Thus, it was inferred that the O_3 pollution was more sensitive to NO_X, and the ZP Park could be qualitatively termed as a NO_X-sensitive area.

The impact of meteorological parameters on pollutant concentrations necessitated an examination of the spatial distribution patterns of key O_3 precursors based on these parameters, as shown in Fig. S1. According to the given analysis, the distributions of those variables are listed in Table 1. The base values were set on the basis of high frequency and average orderly. Finally, the base values of VOCs, NO, NO_2, $PM_{2.5}$, and CO were set at 1.00 mg m^{-3}, 0.010 mg m^{-3}, 0.012 mg m^{-3}, 0.020 mg m^{-3}, and 0.600 mg m^{-3}, respectively. In consideration to the formation conditions of O_3, the base value of the moment was set to 12 o'clock. The meteorological parameters, WD, Temp, RH, and P, were set at the highly frequent 90°, 28 °C, 100/86%, and 101.85 kPa, respectively. In order to mitigate wind-induced dispersion and ensure compliance with the simulation boundary, the WS was set at 0.10 m s^{-1}. Furthermore, for the change of concentration of each pollutant, the base values were uniformly set as 0.001 mg m^{-3} to preserve the metastable state. Consequently, diverse simulation scenarios were established by manipulating the target variables while keeping the remaining factors at their respective base values.

3.2. ANN models

The performance was compared by simultaneously training two ANN models with datasets of D_e and D_g. The evaluation

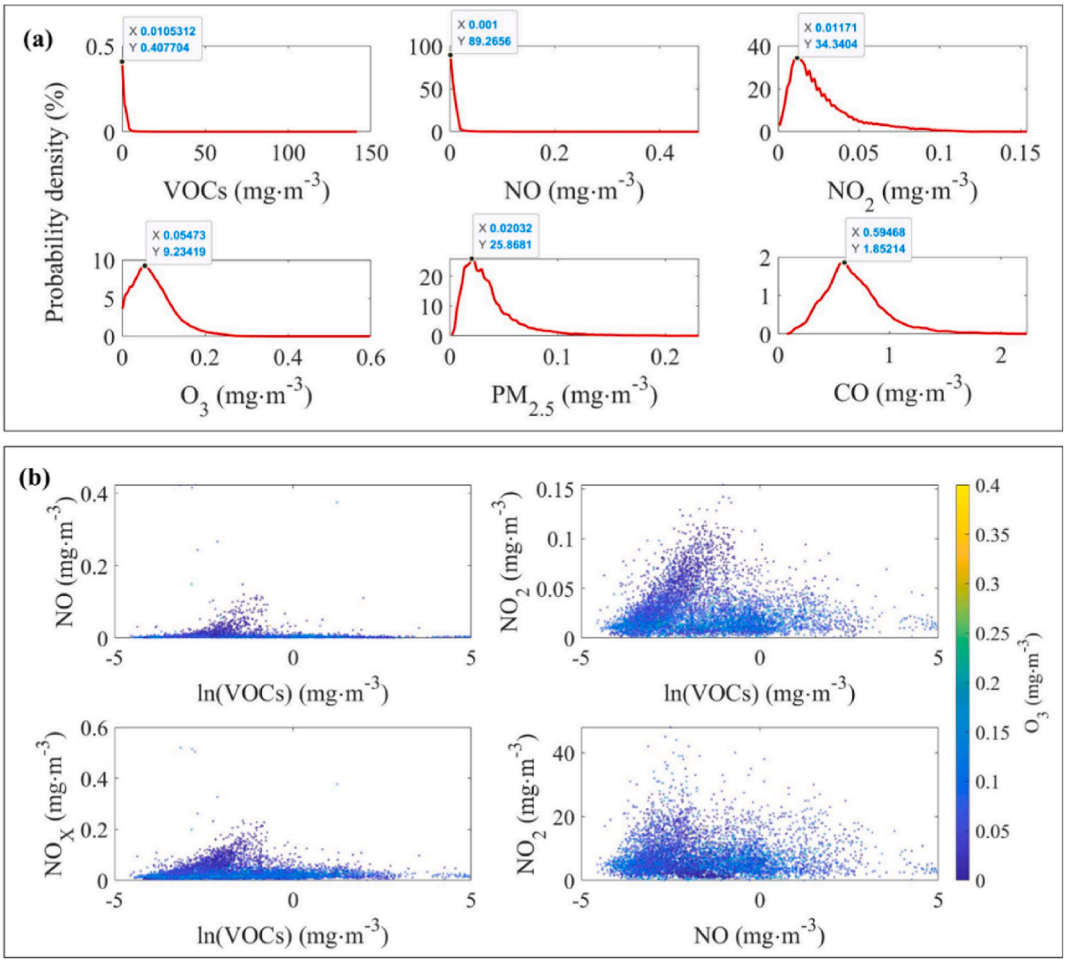

Fig. 2. The distribution of pollutants. (a) The distributions of probability density; (b) Scatter distributions among VOCs and NOx to O_3 concentration.

Table 1
The range and base value of main variables.

Variables	Unit	Average	Min	Max	High frequency	Base value
t	h	–	–	–	–	12
VOCs	mg·m^{-3}	1.14	0.01	141.70	–	1.00
NO	mg·m^{-3}	0.006	0.001	0.474	–	0.010
NO_2	mg·m^{-3}	0.027	0.001	0.154	0.012	0.012
PM	mg·m^{-3}	0.036	0.002	0.231	0.020	0.020
CO	mg·m^{-3}	0.689	0.077	2.234	0.595	0.600
WS	m/s	2.83	0.09	11.27	–	0.10
WD	°	152.811	35.518	315.561	90.000	90
Temp	°C	17.757	−4.299	36.247	28.138	28
RH	%	83.107	21.770	100.000	100.000; 85.919	100; 86
P	kPa	101.302	98.513	103.486	101.845	101.85

parameters, R^2, MSE, MAE, and SSE, were calculated by simulating the two ANN models for 200 times, as shown in Fig. S2. The strong model revealed better performance, with higher R^2, lower MSE, MAE, and SSE than the general one. On average, R^2 increased from 0.901 to 0.922, with the best simulation of 0.926–0.946, respectively. Additionally, the decrease in MSE and MAE was 11.8% and 12.6%, respectively. The average decrease of SSE was from 3.06 to 2.70. Therefore, the addition of moment and the change of concentration of the key pollutants is related to the O_3 formation to a certain extent.

A strong model with relatively good performance was applied for further simulation which was validated by 5-fold cross-validation simulation, as shown in Table S1 and Fig. S3. The evaluation parameters, R^2, MSE, MAE, and SSE, were 0.944, 2.74E-4, 0.0124, and 1.898, respectively. However, for a certain O_3 concentration, when the concentration is relatively low, a slight absolute bias may result in a larger relative error, compared to high concentration. The R^2 values of the simulated O_3 concentrations lower and higher than 0.06 mg m^{-3} were 0.900 and 0.972, respectively. The predicted concentrations of O_3 that were lower than the 0.06 mg m^{-3} were out of the prediction fragment and not discussed which are not the most urgent to be studied. Finally, the change of O_3 concentration was simulated and compared to the observed values. The evaluation parameters, R^2, MSE, MAE, and SSE, were 0.899, 6.33E-5, 5.20E-3, and 0.438, respectively.

3.3. O_3 formation rules

3.3.1. NO and NO_2 to O_3 formation with meteorological parameters

The O_3 concentrations were predicted by the ANN model with different NO and NO_2 concentrations at different meteorological levels. The values of meteorological parameters, WD and WS, were set at 90° and 0.10 m s^{-1}, respectively, which act only on the dispersion of pollutants. The WS was set 0.1 m s^{-1} considering simulation space with enough samples for good prediction and low WS to keep in a relative stable atmospheric condition. The set of 90° was according to the distribution of WD and the high frequency value was chosen, as listed in Table 1. The detailed discussion of the remaining meteorological parameters, Temp, P, and RH, are as follows.

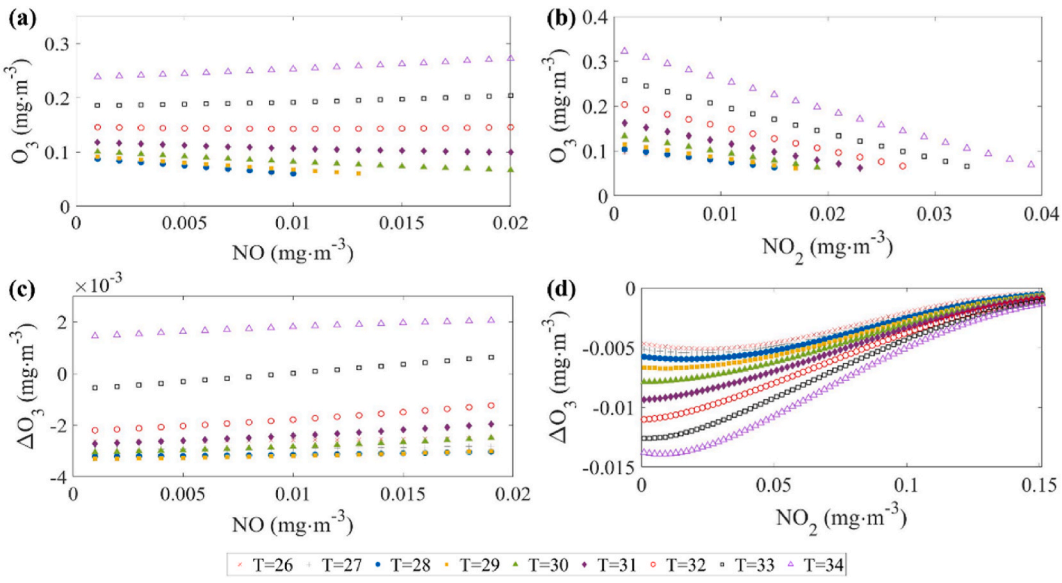

Fig. 3. The O_3 concentrations and concentration change for different Temp. (a) The O_3 concentrations with increasing NO; (b) The O_3 concentrations with increasing NO_2; (c) The O_3 concentrations change with increasing NO; (d) The O_3 concentrations change with increasing NO_2.

3.3.1.1. The effects of temp. The O_3 concentrations and their changes were predicted by the ANN model with different NO and NO_2 concentrations at different Temp. When the Temp increased from 30 °C to 35 °C, the O_3 concentrations increased sharply indicating the significant impact of Temp on photochemical reactions. As shown in Fig. 3 and **S4(a)**, the variation of O_3 concentration for different NO and NO_2 concentrations at different Temp levels was relatively consistent and increased with Temp, which is consistent with the common phenomenon [41,42]. The turning point for O_3 production from elimination due to NO concentration increasing lies within a narrow range around 32 °C. The consistent results of O_3 simulation concentration changes can be attributed to the rapid chemical reaction between NO_X and O_3, as well as the challenge of capturing the reaction process within the 1-h interval of original data for ANN training. Therefore, the atmospheric condition is predominantly lie in transition zones of the positive and negative effect of NO for Temp levels around 32 °C, respectively.

While higher NO_2 concentrations tend to lower the O_3 concentrations across the entire Temp range. The higher Temp tends to increase the capacity for NO_2-mediated O_3 elimination. However, a higher concentration of NO_2 results in weaker O_3 elimination capacity. Besides, Temp has a greater influence on NO_2 than on NO and exhibits a higher absolute incremental reactivity towards O_3 elimination. The high concentration of NO_2 should be considered as being in chemical equilibrium.

3.3.1.2. The effects of P. The O_3 concentrations and changes were also predicted by the ANN model with different NO and NO_2 concentrations and P. According to Fig. 1(c), P is negatively correlated with T basically, while there are diverse pressure ranges at specific temperatures with varying distributions of O_3 concentration. Therefore, the O_3 concentration was simulated at various pressure levels under controlled temperature. Additionally, the NO concentration range was set at 0.001 mg m^{-3} – 0.02 mg m^{-3} with an interval of 0.001 mg m^{-3}. The NO_2 concentration range was set at 0.001 mg m^{-3} – 0.154 mg m^{-3} with an interval of 0.002 mg m^{-3}, and the range of P was set at 99.5 kPa–103 kPa to cover nearly the whole range of the original data. As shown in Fig. 4, the influence of P on O_3 concentrations is complicated, showing inconsistency for different NO concentrations. Overall, the peak of O_3 concentration is reached at 101.0 kPa, within the entire NO concentration range. Interestingly, the change in O_3 concentration appeared relatively constant with different levels of NO concentration. When P exceeds 100 kPa, the decrease in O_3 concentration becomes more pronounced, and this effect is further amplified at a pressure of 103.0 kPa, indicating the O_3 concentration tends to decrease and exhibits a greater capacity for reduction at high P when NO is introduced into the atmosphere. The capacity of higher pressure to decrease O_3 concentrations is enhanced due to its association with improved diffusion.

The peaks of O_3 concentration appear at 101.5 kPa and 99.5 kPa in the regions of low and high NO_2 concentrations. Additionally, the O_3 concentration decreases sharply with the increase in NO_2 concentration when P is larger than 101.0 kPa, resulting in high O_3 concentration appearing at low NO_2 concentration. When a NO_2 concentration of 0.002 mg m^{-3} is added to each system, the O_3 concentration shows an overall decrease, and the capacity of decrease tends to get smaller with the increase in NO_2 concentration. The impact of P on O_3 concentration can be attributed in the different diffusion conditions of atmospheric and air boundary layers. Besides, compared to the influence from Temp, that of pressure were relatively weak.

3.3.1.3. The effects of RH. The influence of RH on O_3 concentrations also shows inconsistency for different NO concentrations, as shown in Fig. 5. The O_3 concentration reaches the peak at 40% within the entire range of NO concentration, while the decrease of O_3

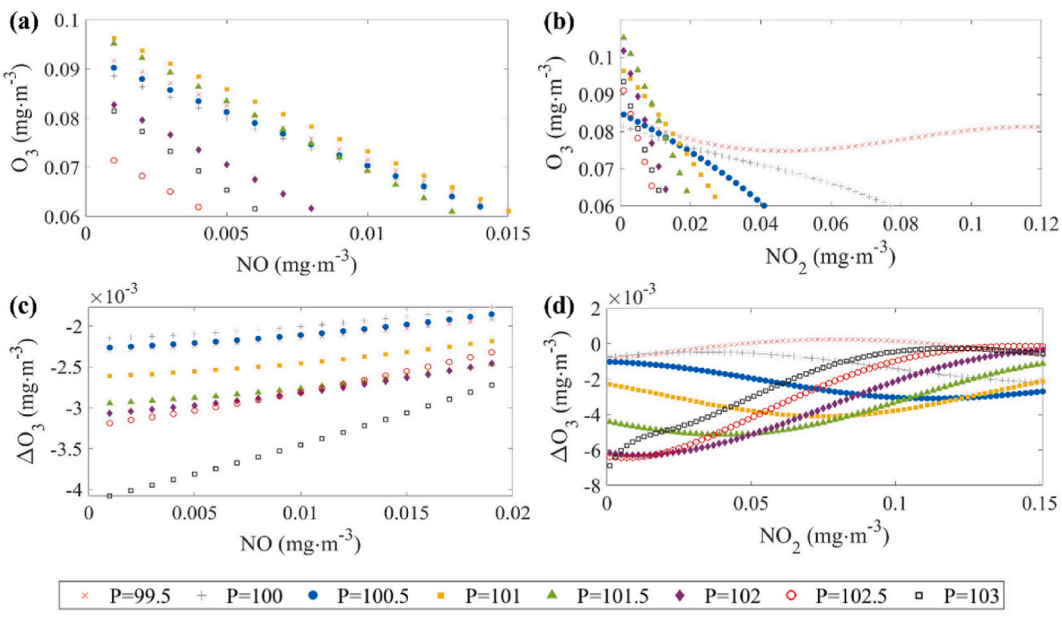

Fig. 4. The O_3 concentrations and concentration change for different P. (a) The O_3 concentrations with increasing NO; (b) The O_3 concentrations with increasing NO_2; (c) The O_3 concentrations change with increasing NO; (d) The O_3 concentrations change with increasing NO_2.

concentration appears to be smaller for different NO concentrations when RH is higher than 60%. The O_3 concentration appears to decrease linearly with the increase in NO concentration when RH is 60%. Additionally, when the RH reaches saturation, the O_3 concentration distribution turns gently inconsistent. The O_3 concentration tends to decrease and has a larger decrease capacity at medium to low RH by adding NO into the atmosphere. Furthermore, a smaller interval of RH in the range of 32%–50% was investigated, as shown in Fig. S5. The O_3 concentration shows a very small decrease with the increase in NO concentration with the peak appears at 40% and 32% for lower and higher NO concentration, respectively. The O_3 concentration also decreases with the increase in NO_2 concentration, and the decrease is sharper for higher RH. When NO_2 concentration is lower than 0.11 mg m^{-3}, the decrease becomes larger with RH. However, it is the opposite for NO_2 concentration higher than 0.11 mg m^{-3}.

3.3.1.4. The combined effects of RH and P. Since the O_3 formation rules by RH and P [43] are complex, the precursors with different concentration levels showed different affection on O_3 concentration under different RH and P conditions, the joint analysis of RH and P was conducted. The combined effects on O_3 concentrations were further analyzed by fixing other variables at general levels, as shown in Fig. S6(a). The contour chart is a convenient visual method for quickly estimating O_3 concentration based on real-time conditions. The high O_3 concentrations centers at the lower left area, which show a certain extent of skewing at different NO_X concentrations. Therefore, lower P and lower or median RH result in higher O_3 concentrations. The contour curves show fluctuation to a certain extent which may be due to factors that have not been considered in this study, like solar radiation intensity and cloud age [44–46].

Additionally, the combined effects between RH and Temp were also calculated, as shown in Fig. S6(b). The O_3 concentrations reveal consistently located at top right corner of high RH and high Temp, and the increase in O_3 concentrations become sharper at higher Temp. For the combined effects between P and Temp, RH at 100% and 86% were both evaluated, as shown in Fig. S6(c) and **(d)**. When Temp is higher than 30 °C, the O_3 concentrations increase sharply which effect little by P.

3.3.2. VOCs–NO_2 to O_3 formation with meteorological parameters

The O_3 concentrations reflected with the concentration changes of VOCs and NO_2 at different atmospheric conditions is a complex process [47]. Although the concentration of VOCs is a complex variable, containing many species with different chemical reactivity, the applied model showed good simulation performances with VOCs due to the relatively stable industrial structure in a mature industrial park. The contour curves of O_3 concentration at each condition were plotted within the local concentration ranges of VOCs and NO_2. Unlike the EKMA curve [48], which expresses the O_3 isopleth corresponding to different concentrations of VOCs and NO_X based on photochemical reaction and meteorological diffusion on a certain day [22], the contour curves express the general performance at a certain Temp, RH, P, and relatively stable atmospheric conditions. Significantly, since the concentration range of VOCs is much larger than that of NO_X, the O_3 isopleths are almost intuitive and may be more suitable for controlling local O_3. Furthermore, the O_3 isopleths are intuitively relatively consistent for different concentrations of VOCs and NO_X, indicating that the local O_3 concentration in the area was controlled mainly by NO_X concentration in the simulation space. Furthermore, each contour figure was converted to an arrow directing to the increase in O_3 concentration. As shown in Fig. S7, the contour curves of O_3 concentration at different Temp levels with 100% RH and 103 kPa P were also integrated below the arrows. There is a relatively strong influence of RH and P on the sensitivities of VOCs and NO_X, with limited impact from Temp. Under lower RH conditions of 20% and 50%, the O_3 concentration exhibited

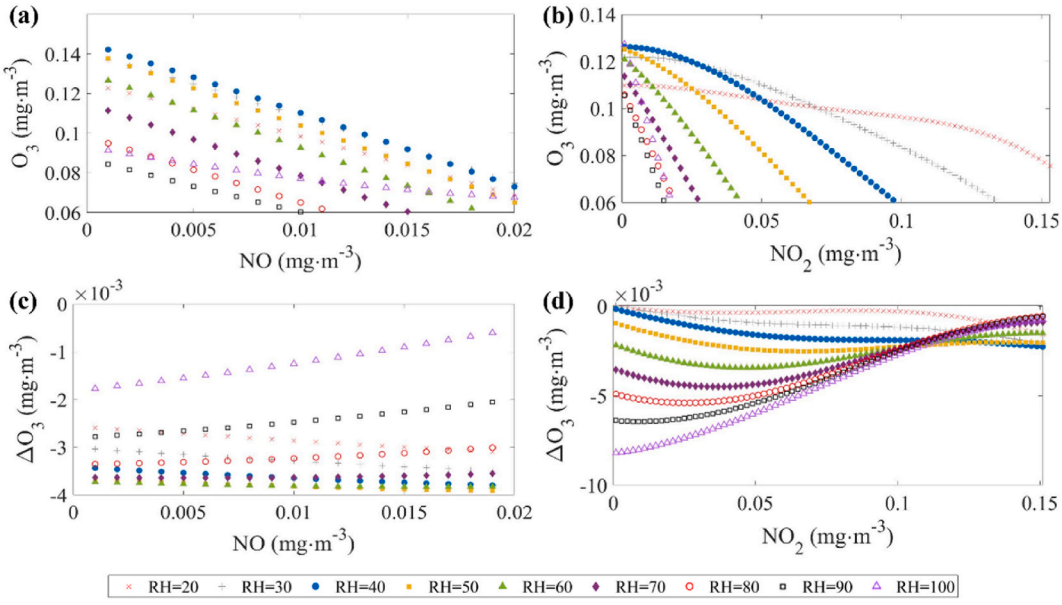

Fig. 5. The O_3 concentrations and concentration change for different RH. (a) The O_3 concentrations with increasing NO; (b) The O_3 concentrations with increasing NO_2; (c) The O_3 concentrations change with increasing NO; (d) The O_3 concentrations change with increasing NO_2.

sensitivity to NO_X, decreasing as NO_X concentration increased.

The nonlinear and inter-effected relationships of VOCs and NO_X on O_3 pollution are complicated [4,49]. The influence of VOCs and NO_X on O_3 pollution was investigated at high-frequency meteorology and high O_3 concentration conditions. The high-frequency meteorological conditions refer to the meteorological conditions that mostly likely to occur, which were built with high-frequency meteorological elements of Temp, P, and RH, setting at 28 °C, 101.85 kPa, and 100%, according to the distribution of each variable and the high frequency value. However, the Temp, P, and RH are set at 34 °C, 103.00 kPa, and 100%, respectively, for high O_3 concentration conditions based on O_3 concentration analysis above. The O_3 concentration is strongly sensitive to NO_2 for both conditions, as shown in Fig. 6(a) and Fig. 6(b), which increased with the decrease in the concentration of NO_X, as the vertical coordinate of the concentration of NO_X was smaller than the horizontal coordinate of the concentration of VOCs with orders of magnitude. A more detailed analysis has been discussed further with the contour curves at high-frequency meteorology and high O_3 concentration conditions based on the simulation results of the ANN models for further exploration.

IR_{NOx} and IR_{VOCs} were calculated based on simulation results. Though the IR_{NOx} and IR_{VOCs} were calculated with the predicted concentrations of pollutants, considering the enough samples and distribution analysis of each variable, the ANN model revealed high performance in both the train set and test set. Thus, the predicted concentrations of pollutants were under control, so were the calculation of IR_{NOx} and IR_{VOCs}. Since the variables were controlled for O_3 concentration prediction, the IR_{NOx} and IR_{VOCs} reflect the O_3 increasing capacity of NOx and VOCs individually.

3.3.2.1. High-frequency meteorology conditions. Further analysis found that the changes of IR_{NOx} and IR_{VOCs} were relatively consistent for different concentrations of VOCs at high-frequency meteorology conditions. Therefore, IR_{NOx} and IR_{VOCs} were plotted for different concentrations of VOCs. As shown in Fig. 7(a), IR_{NOx} of different concentrations of NOx, in the range of 0.001 mg m^{-3} – 0.147 mg m^{-3} at different concentrations of VOCs, were calculated. The IR_{NOx} values were consistently negative, ranging from −4.42 to −0.41, indicating that even a slight reduction in NOx could lead to an increase in O_3 concentration. These findings suggest that the atmospheric conditions fall within the NOx-titration region [50]. Additionally, IR_{NOx} increased with the increase in the concentration of NOx and showed little difference at different concentrations of VOCs. The range of IR_{NOx} became slightly larger with the increase in concentrations of VOCs from (−4.1 ~ −0.41) to (−4.42 ~ −0.51). Hence, IR_{NOx} was almost controlled by the concentration of NOx, corresponding to the total reaction, $NO_2 + O_2 \overset{h\nu, R}{\Leftrightarrow} NO + O_3$.

Meanwhile, IR_{VOCs} also showed a relatively constant trend for different concentrations of VOCs and a weak positive effect on O_3 concentrations in the range of 4.32E-4 – 2.33E-3. However, the change in the range of IR_{VOCs} was narrower with the increase in the concentrations of VOCs. Moreover, for each concentration of VOCs, the results showed a minimum IR_{VOCs}, located in the range of concentrations of NOx between 0.041 mg m^{-3} to 0.049 mg m^{-3}. Though the peak of IR_{VOCs} increased with the increase in the concentrations of VOCs, the maximum IR_{VOCs} was still limited at a lower level. Interestingly, the minimum IR_{VOCs} expressed a strong linear relationship with the concentrations of VOCs for R^2, reaching 0.99995, as shown in Fig. 7(b) and **8(a)**. Therefore, a minimum incremental reactivity (MinIR) exists at certain concentrations of VOCs for different concentrations of NOx. MinIR linearly increases with the increase in the concentrations of VOCs.

Furthermore, comparing IR_{VOCs} and IR_{NOx} can explore the sensitivities of VOCs and NOx on O_3 formation. The trends between IR_{VOCs} and IR_{NOx} are also relatively constant at different concentrations of VOCs. Therefore, the curves were shown at intervals of concentrations of VOCs for better visibility, as shown in Fig. 7(c). Since the absolute value of IR_{NOx} is much larger than IR_{VOCs}, the ratio of IR_{VOCs} to IR_{NOx} was in the range of −5.17E-3 – (−1.28E-4). Therefore, the studied area belongs to a NOx-sensitive region at high-frequency conditions, which is consistent with the previous analysis of distribution characteristics.

However, the concentrations of VOCs and NOx do not imply that the emission control of NO_X should be prioritized over the emission control of VOCs. On the contrary, the concentrations of VOCs are at a relatively high oversaturation level, so more effort should be focused on their control. Additionally, higher concentrations of VOCs resulted in higher IR_{VOCs}. IR_{VOCs} had a relatively lower effect on O_3 concentration when IR_{NOx} was located between 0.033 mg m^{-3} – 0.037 mg m^{-3}. The higher concentrations of NOx revealed a higher absolute ratio of IR_{VOCs} to IR_{NOx} for certain concentrations of VOCs, as shown in Fig. 8(b).

3.3.2.2. High O_3 concentration condition. The changes of IR_{NOx} and IR_{VOCs} were relatively consistent for different concentrations of

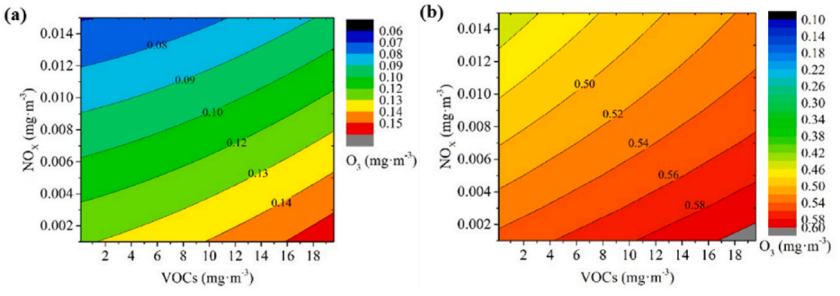

Fig. 6. The isopleths of O_3 concentration. (a) at high frequent meteorology condition; (b) at high O_3 concentration condition.

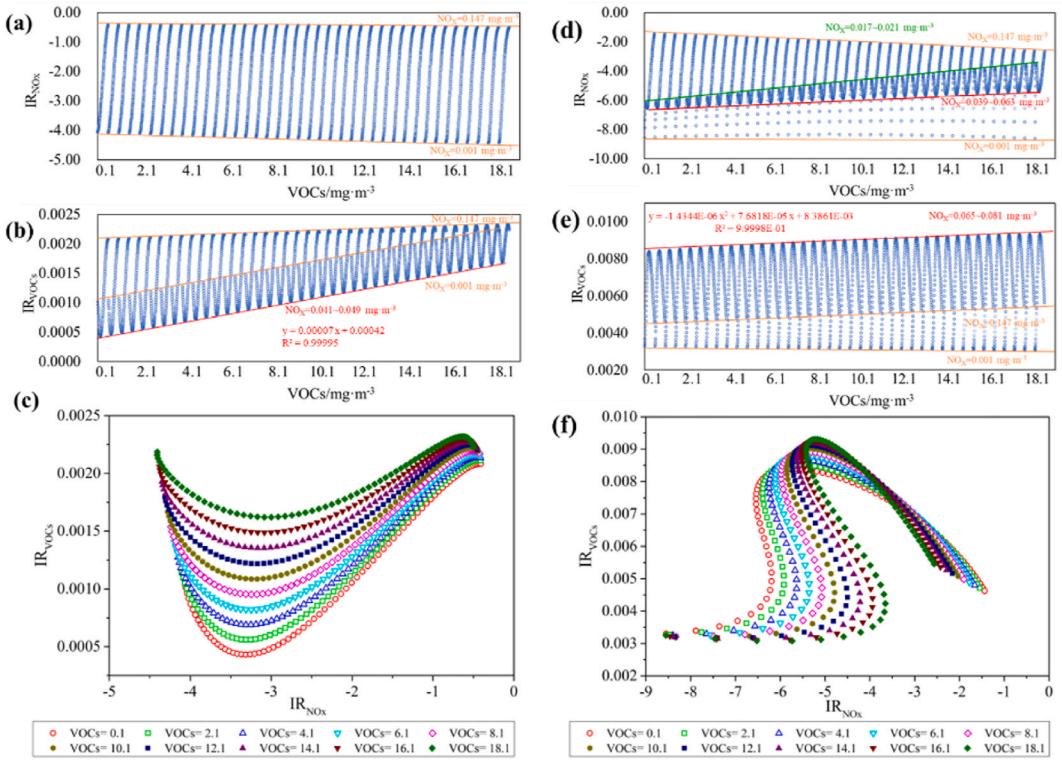

Fig. 7. IR_{NOx}, IR_{VOCs}, and their comparison. (a) IR_{NOx} at high-frequency meteorology conditions; (b) IR_{VOCs} at high-frequency meteorology conditions; (c) comparison between IR_{NOx} and IR_{VOCs} at high-frequency meteorology conditions; (d) IR_{NOx} at high O_3 concentration conditions; (e) IR_{VOCs} at high O_3 concentration conditions; (f) comparison between IR_{NOx} and IR_{VOCs} at high O_3 concentration conditions.

VOCs at high O_3 concentration conditions. As shown in Fig. 7(d), IR_{NOx} is smaller than 0, in the range of −8.61 – (−1.44), which is relatively higher than that in high-frequency meteorology conditions. Therefore, this implies that despite the presence of a high O_3 concentration, NOx exhibits a relatively stronger titration effect on O_3 levels. Moreover, unlike the high-frequency meteorology conditions, the increase in IR_{NOx} was not simple, but a peak and a valley existed in each curve. At different concentrations of VOCs, the

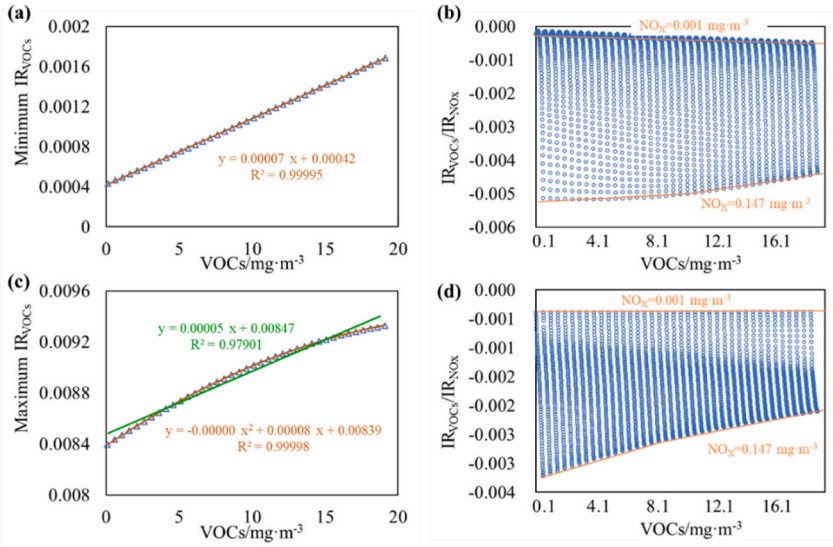

Fig. 8. The maximum IR_{VOCs} and the ratio of IR_{VOCs} to IR_{NOx}. (a) the maximum IR_{VOCs} at high frequent meteorology conditions; (b) the ratio of IR_{VOCs} to IR_{NOx} at high frequent meteorology conditions; (c) the maximum IR_{VOCs} at high O_3 concentration conditions; (d) the ratio of IR_{VOCs} to IR_{NOx} at high O_3 concentration conditions.

peaks occurred for the concentrations of NOx in the range of 0.017 mg m^{-3} – 0.021 mg m^{-3}. Additionally, the occurrence point shifted slightly to the higher concentrations of NOx, and IR_{NOx} increased with the increase in the concentration of VOCs. Meanwhile, a valley was observed in the concentration of NOx ranging from 0.039 to 0.063 mg m^{-3}. Hence, it can be inferred that the reactions under high O_3 concentration conditions were more complex than at the high-frequency meteorology conditions, which may process different photochemical reactions.

IR_{VOCs} also showed a relatively constant trend for different concentrations of VOCs and a weak positive effect on O_3 concentrations in the range of 3.06E-3 - 9.33E-3. However, the change in the range of IR_{VOCs} was larger with the increase in the concentrations of VOCs. Interestingly, for each concentration of VOCs, the results showed a maximum IR_{VOCs}, located in the concentration range of NOx between 0.065 mg m^{-3}–0.081 mg m^{-3}. Moreover, the maximum IR_{VOCs} expressed a straight linear relationship with R^2 equal to 0.979 and a strong linear relationship with the concentration of VOCs as R^2 reached 0.99998, as shown in Fig. 7(e) and **8(c)**. Therefore, it can be inferred that high concentrations of O_3 lead to the existence of a local maximum incremental reactivity (MIR_L) for different levels of NOx at specific concentrations of VOCs. Furthermore, MIR_L exhibits a linear increase with rising VOC concentrations. The MIR_L has a range of 8.40E-3 – 9.33E-3, significantly smaller than the general applied MIR [15,16] of each VOC species. Therefore, due to the limited capacity of O_3 formation under atmospheric conditions characterized by high VOCs concentrations, the application of MIR for evaluating OFP may lead to a significant overestimation of O_3 formation. Consequently, it is more appropriate to utilize statistically simulated local-reachable MIR_L for a specific geographical area.

Furthermore, the comparison between IR_{VOCs} and IR_{NOx} was analyzed. The trends between IR_{VOCs} and IR_{NOx} were relatively consistent for different concentrations of VOCs. Thus, the curves were shown at the intervals of the concentrations of VOCs for better visibility, as shown in Fig. 7(d). Since the absolute value of IR_{NOx} is much larger than IR_{VOCs}, the ratio of IR_{VOCs} to IR_{NOx} is in the range of −3.22E-3 – (−3.80E-4). Therefore, the studied area also belonged to a NOx-sensitive region at high O_3 concentrations. The relationship between IR_{VOCs} and IR_{NOx} is complicated for certain concentrations of VOCs, as shown in Fig. 7(f). Additionally, the ratio of IR_{VOCs} to IR_{NOx} showed a consistent decrease with the increase in the concentrations of NOx, as shown in Fig. 8(d).

4. Uncertainty discussion and conclusion

4.1. Uncertainty discussion

The O_3 pollution formation is influenced by many factors, with the VOCs and NOx as the dominant precursors and the warm weather and low WS as major meteorological factors [51,52]. The ANN model showed a good simulation performance in many data disposal fields and prediction of O_3 formation [53,54]. However, in comparison to the ground-based monitoring of pollutant concentrations, the simulated O_3 concentration from ANN still exhibits some disparities, partly attributable to uncertainties in observations, simulation parameter settings, assumed factors influencing O_3 formation, and simulation ranges. Another portion was derived from the primary dataset, though most affection factors were taken into consideration. There were still other factors out of the primary dataset, such as solar radiation intensity, cloud cover, and also the chemical reactions of different VOC species.

There are many approaches to keep the uncertainties under control, which are as follows.

(1) For better simulation performance: The data from local hourly monitoring for a year were applied to afford enough samples for training the ANN model. The input variables were expended with the moment and the concentration changes of pollutants in each sample. Additionally, the evaluation parameters, R^2, MSE, MAE, and SSE, were calculated to control the performance of the trained model.
(2) For the accuracy of simulation results: The distribution characteristics were analyzed before application in mechanism exploration, to ensure that the simulation was within the variable space of enough original samples due to the complexity of the O_3 formation process. Additionally, the meteorological factors were set relatively stable atmospheric conditions and consistent within the variable space.

4.2. Conclusion

Based on the controllable uncertainty simulation, some credible conclusions that can be drawn are as follows.

(1) The ANN model demonstrated superior simulation performance for all evaluation parameters of R^2, MSE, MAE, and SSE by incorporating the variations in moment and concentration of pollutants with respect to general meteorological factors and pollutant concentrations. R^2 value increased from 0.901 to 0.922, MSE and MAE decreased by 11.8% and 12.6%, respectively, and SSE decreased from 3.06 to 2.70, averagely.
(2) The local atmospheric conditions were characteristic of a NOx-titration region, where elevated Temp levels enhanced the photochemical reactions. These reactions exhibited an increasing trend with the increase in Temp and became significant when the Temp exceeded 30 °C. Furthermore, higher Temp tended to enhance the capacity of NO_2 for O_3 elimination, while elevated concentrations of NO_2 lead to a reduction in the capacity of eliminating O_3. Therefore, the concentration of O_3 tends to decrease and exhibits a greater capacity for reduction at high P, low Temp, and medium to low RH when NO is introduced into the atmosphere. However, the O_3 concentration also tends to decrease and demonstrates a larger potential for reduction at medium P, high Temp, and high RH when NO_2 is added to the atmospheric mixture. The sensitivities of VOCs and NO_X on O_3 formation were significantly influenced by RH and P.

(3) The IR_{VOCs} exhibited significantly lower levels compared to the IR_{NOx} in this highly VOCs-polluted region. Under high-frequency meteorology conditions, elevated concentrations of VOCs led to increased levels of both IR_{VOCs} and IR_{NOx}. The MinIR exhibited a robust linear correlation with increasing concentrations of VOCs at each NOx concentration. At high O_3 concentrations, despite the presence of elevated O_3 levels, NOx exhibits a relatively stronger titration effect on O_3 concentration. The reactions under high O_3 concentration conditions are characterized by increased complexity compared to those occurring during high-frequency meteorological events, potentially involving distinct photochemical pathways. The MIR_L exhibited a linear increase with the concentration of VOCs at specific levels, corresponding to different concentrations of NOx. Moreover, considering the limited O_3 formation capacity of VOCs, it is noteworthy that the MIR would lead to a significant overestimation of attainable O_3 levels in NOx-sensitive regions. Therefore, the statistically simulated local-reachable MIR_L may be more suitable and practical for NOx-sensitive regions than direct application of MIR.

According to the quantified response to the changes in meteorological elements and precursors concentrations, the established O_3 formation rules can significantly support local management strategies for controlling VOCs and NOx emissions, effectively guiding rapid responses to O_3 pollution and ensuring air quality.

In this study, the concentrations of VOCs were set as a singular feature, comprehensive and intuitive representations were employed to derive relative rules by variable-controlled ANN simulation on O_3 concentration. Therefore, future studies can further employ machine learning approaches to investigate the response to continuous changes in controlled variables, aiming to effectively control local O_3 pollution and improve air quality. Additionally, it is recommended that future research extends this method to simulate the local MIR_L of each VOC species, enabling more precise and targeted management strategies.

Funding statement

This work was supported by the National Key Research and Development Program of China (No. 2022YFC3703500) and the Public Welfare Application Research Project of Huzhou (No. 2022GZ61).

Author contribution statement

Qiaoli Wang: conceived and designed the experiments; performed the experiments; analyzed and interpreted the data; wrote the paper. Dongping Sheng: performed the experiments; analyzed and interpreted the data; contributed reagents, materials, analysis tools or data. Chengzhi Wu; Jingkai Zhao; Shengdong Yao: contributed reagents, materials, analysis tools or data. Feili Li; Xiaojie Ou: performed the experiments; analyzed and interpreted the data. Wei Li; Jianmeng Chen: conceived and designed the experiments; contributed reagents, materials, analysis tools or data.

Data availability statement

The data that has been used is confidential.

Declaration of competing interest

The authors declare that they have no known competing financial interests or personal relationships that could have appeared to influence the work reported in this paper.

Appendix A. Supplementary data

Supplementary data to this article can be found online at https://doi.org/10.1016/j.heliyon.2023.e20125.

References

[1] K. Li, D.J. Jacob, L. Shen, X. Lu, I. De Smedt, H. Liao, Increases in surface ozone pollution in China from 2013 to 2019: anthropogenic and meteorological influences, Atmos. Chem. Phys. 20 (19) (2020) 11423–11433, https://doi.org/10.5194/acp-20-11423-2020.

[2] C. He, X. Lu, H. Wang, H. Wang, Y. Li, G. He, Y. He, Y. Wang, Y. Zhang, Y. Liu, Q. Fan, S. Fan, The unexpected high frequency of nocturnal surface ozone enhancement events over China: characteristics and mechanisms, Atmos. Chem. Phys. 22 (23) (2022) 15243–15261, https://doi.org/10.5194/acp-22-15243-2022.

[3] D. Jing, N. Cheng, C. Zhang, Z. Chen, X. Cai, S. Li, J. Zhao, Q. Wang, W. Li, A novel approach for VOC source apportionment combining characteristic factor and pattern recognition technology in a Chinese industrial area, J. Environ. Sci. 121 (2022) 25–37, https://doi.org/10.1016/j.jes.2021.08.056.

[4] C. Chen, T. Chen, S. Huang, K. Chang, Comparison of the RADM2 and RACM chemical mechanisms in O3 simulations: effect of the photolysis rate constant, Sci. Rep. 11 (1) (2021) 5024, https://doi.org/10.1038/s41598-021-84629-4.

[5] H. Lu, X. Lyu, H. Cheng, Z. Ling, H. Guo, Overview on the spatial-temporal characteristics of the ozone formation regime in China, Environmental Science-Processes & Impacts 21 (6) (2019) 916–929, https://doi.org/10.1039/c9em00098d.

[6] Y. Gu, F. Yan, J. Xu, Y. Qu, W. Gao, F. He, H. Liao, A measurement and model study on ozone characteristics in marine air at a remote island station and its interaction with urban ozone air quality in Shanghai, China, Atmos. Chem. Phys. 20 (22) (2020) 14361–14375, https://doi.org/10.5194/acp-20-14361-2020.

[7] S. Gong, L. Zhang, C. Liu, S. Lu, W. Pan, Y. Zhang, Multi-scale analysis of the impacts of meteorology and emissions on PM2.5 and O3 trends at various regions in China from 2013 to 2020 2. Key weather elements and emissions, Sci. Total Environ. 824 (2022), 153847, https://doi.org/10.1016/j.scitotenv.2022.153847.

[8] R. Wang, X. Wang, S. Cheng, K. Wang, L. Cheng, J. Zhu, H. Zheng, W. Duan, Emission characteristics and reactivity of volatile organic compounds from typical high-energy-consuming industries in North China, Sci. Total Environ. 809 (2022), 151134, https://doi.org/10.1016/j.scitotenv.2021.151134.

[9] J. Mei, Y. Shen, Q. Wang, Y. Shen, W. Li, J. Zhao, J. Chen, S. Zhang, Roles of oxygen species in low-temperature catalytic o-xylene oxidation on MOF-derived bouquetlike CeO(2), ACS Appl. Mater. Interfaces 14 (31) (2022) 35694–35703, https://doi.org/10.1021/acsami.2c08418.

[10] J. Zhao, J. Gao, X. Jin, J. You, K. Feng, J. Ye, J. Chen, S. Zhang, Superior dimethyl disulfide degradation in a microbial fuel cell: extracellular electron transfer and hybrid metabolism pathways, Environ. Pollut. 315 (2022), 120469, https://doi.org/10.1016/j.envpol.2022.120469.

[11] J. Zhao, K. Feng, Y. Lu, Z. Cheng, J. Ye, Y. Shen, J. Hu, J. Chen, S. Zhang, W. Li, 3D pore-matched PANI@CNT bioanode for efficient electron extraction from toluene, J. Power Sources 536 (2022), 231509, https://doi.org/10.1016/j.jpowsour.2022.231509.

[12] W. Wei, S. Cheng, G. Li, G. Wang, H. Wang, Characteristics of ozone and ozone precursors (VOCs and NOx) around a petroleum refinery in Beijing, China, J. Environ. Sci. 26 (2) (2014) 332–342, https://doi.org/10.1016/s1001-0742(13)60412-x.

[13] W. Wei, Z.F. Lv, Y. Li, L.T. Wang, S. Cheng, H. Liu, A WRF-Chem model study of the impact of VOCs emission of a huge petro-chemical industrial zone on the summertime ozone in Beijing, China, Atmos. Environ. 175 (2018) 44–53, https://doi.org/10.1016/j.atmosenv.2017.11.058.

[14] Q. Wang, D. Sheng, C. Wu, D. Jing, N. Cheng, X. Cai, S. Li, J. Zhao, W. Li, J. Chen, A supplementary assessment system of AQI-V for comprehensive management and control of air quality in chemical industrial parks, J. Environ. Sci. 130 (2023) 114–125, https://doi.org/10.1016/j.jes.2022.06.037.

[15] Q. Wang, S. Li, M. Dong, W. Li, X. Gao, R. Ye, D. Zhang, VOCs emission characteristics and priority control analysis based on VOCs emission inventories and ozone formation potentials in Zhoushan, Atmos. Environ. 182 (2018) 234–241, https://doi.org/10.1016/j.atmosenv.2018.03.034.

[16] N. Cheng, D. Jing, C. Zhang, Z. Chen, W. Li, S. Li, Q. Wang, Process-based VOCs source profiles and contributions to ozone formation and carcinogenic risk in a typical chemical synthesis pharmaceutical industry in China, Sci. Total Environ. 752 (2021), 141899, https://doi.org/10.1016/j.scitotenv.2020.141899.

[17] N. Cheng, C. Zhang, D. Jing, W. Li, T. Guo, Q. Wang, S. Li, An integrated chemical mass balance and source emission inventory model for the source apportionment of PM2.5 in typical coastal areas, J. Environ. Sci. (China) 92 (2020) 118–128, https://doi.org/10.1016/j.jes.2020.01.018.

[18] C. Zhang, D. Jing, C. Wu, S. Li, N. Cheng, W. Li, G. Wang, B. Chen, Q. Wang, J. Hu, Integrating chemical mass balance and the community multiscale air quality models for source identification and apportionment of PM2.5, Process Saf. Environ. Protect. 149 (2021) 665–675, https://doi.org/10.1016/j.psep.2021.03.033.

[19] H. Qu, Y. Wang, R. Zhang, X. Liu, L.G. Huey, S. Sjostedt, L. Zeng, K. Lu, Y. Wu, M. Shao, M. Hu, Z. Tan, H. Fuchs, S. Broch, A. Wahner, T. Zhu, Y. Zhang, Chemical production of oxygenated volatile organic compounds strongly enhances boundary-layer oxidation chemistry and ozone production, Environ. Sci. Technol. 55 (20) (2021) 13718–13727, https://doi.org/10.1021/acs.est.1c04489.

[20] M.A. Venecek, W.P.L. Carter, M.J. Kleeman, Updating the SAPRC maximum incremental reactivity (MIR) scale for the United States from 1988 to 2010, J. Air Waste Manag. Assoc. 68 (12) (2018) 1301–1316, https://doi.org/10.1080/10962247.2018.1498410.

[21] W. Pan, S. Gong, K. Lu, L. Zhang, S. Xie, Y. Liu, H. Ke, X. Zhang, Y. Zhang, Multi-scale analysis of the impacts of meteorology and emissions on PM(2.5) and O(3) trends at various regions in China from 2013 to 2020 3. Mechanism assessment of O(3) trends by a model, Sci. Total Environ. 857 (Pt 3) (2023), 159592, https://doi.org/10.1016/j.scitotenv.2022.159592.

[22] Z. Tan, K. Lu, H. Dong, M. Hu, X. Li, Y. Liu, S. Lu, M. Shao, R. Su, H. Wang, Y. Wu, A. Wahner, Y. Zhang, Explicit diagnosis of the local ozone production rate and the ozone-NOx-VOC sensitivities, Sci. Bull. 63 (16) (2018) 1067–1076, https://doi.org/10.1016/j.scib.2018.07.001.

[23] Z. Tan, K. Lu, M. Jiang, R. Su, H. Dong, L. Zeng, S. Xie, Q. Tan, Y. Zhang, Exploring ozone pollution in Chengdu, southwestern China: a case study from radical chemistry to O3-VOC-NOx sensitivity, Sci. Total Environ. 636 (2018) 775–786, https://doi.org/10.1016/j.scitotenv.2018.04.286.

[24] K. Lu, S. Guo, Z. Tan, H. Wang, D. Shang, Y. Liu, X. Li, Z. Wu, M. Hu, Y. Zhang, Exploring atmospheric free-radical chemistry in China: the self-cleansing capacity and the formation of secondary air pollution, Natl. Sci. Rev. 6 (3) (2019) 579–594, https://doi.org/10.1093/nsr/nwy073.

[25] A. Kumar, R.S. Patil, A.K. Dikshit, S. Islam, R. Kumar, Evaluation of control strategies for industrial air pollution sources using American meteorological society/environmental protection agency regulatory model with simulated meteorology by weather research and forecasting model, J. Clean. Prod. 116 (2016) 110–117, https://doi.org/10.1016/j.jclepro.2015.12.079.

[26] J. Wang, L. Bai, S. Wang, C. Wang, Research and application of the hybrid forecasting model based on secondary denoising and multi-objective optimization for air pollution early warning system, J. Clean. Prod. 234 (2019) 54–70, https://doi.org/10.1016/j.jclepro.2019.06.201.

[27] K. Shukla, N. Dadheech, P. Kumar, M. Khare, Regression-based flexible models for photochemical air pollutants in the national capital territory of megacity Delhi, Chemosphere 272 (2021), 129611, https://doi.org/10.1016/j.chemosphere.2021.129611.

[28] H. Liu, Y. Xu, C. Chen, Improved pollution forecasting hybrid algorithms based on the ensemble method, Appl. Math. Model. 73 (2019) 473–486, https://doi.org/10.1016/j.apm.2019.04.032.

[29] S. Du, T. Li, Y. Yang, S.-J. Horng, Deep air quality forecasting using hybrid deep learning framework, IEEE Trans. Knowl. Data Eng. 33 (6) (2021) 2412–2424, https://doi.org/10.1109/tkde.2019.2954510.

[30] J. Kim, X. Wang, C. Kang, J. Yu, P. Li, Forecasting air pollutant concentration using a novel spatiotemporal deep learning model based on clustering, feature selection and empirical wavelet transform, Sci. Total Environ. 801 (2021), 149654, https://doi.org/10.1016/j.scitotenv.2021.149654.

[31] A. Sayeed, Y. Choi, E. Eslami, Y. Lops, A. Roy, J. Jung, Using a deep convolutional neural network to predict 2017 ozone concentrations, 24 hours in advance, Neural Network. 121 (2020) 396–408, https://doi.org/10.1016/j.neunet.2019.09.033.

[32] X. Su, J. An, Y. Zhang, P. Zhu, B. Zhu, Prediction of ozone hourly concentrations by support vector machine and kernel extreme learning machine using wavelet transformation and partial least squares methods, Atmos. Pollut. Res. 11 (6) (2020) 51–60, https://doi.org/10.1016/j.apr.2020.02.024.

[33] X. Xu, M. Yoneda, Multitask air-quality prediction based on LSTM-autoencoder model, IEEE Trans. Cybern. 51 (5) (2021) 2577–2586, https://doi.org/10.1109/TCYB.2019.2945999.

[34] A. Yafouz, A.N. Ahmed, N.a. Zaini, A. El-Shafie, Ozone concentration forecasting based on artificial intelligence techniques: a systematic review, water, air, & Soil Pollution 232 (2) (2021), https://doi.org/10.1007/s11270-021-04989-5.

[35] R. Feng, H.J. Zheng, A.R. Zhang, C. Huang, H. Gao, Y.C. Ma, Unveiling tropospheric ozone by the traditional atmospheric model and machine learning, and their comparison:A case study in hangzhou, China, Environ. Pollut. 252 (Pt A) (2019) 366–378, https://doi.org/10.1016/j.envpol.2019.05.101.

[36] R. Feng, H.-j. Zheng, H. Gao, A.-r. Zhang, C. Huang, J.-x. Zhang, K. Luo, J.-r. Fan, Recurrent Neural Network and random forest for analysis and accurate forecast of atmospheric pollutants: a case study in Hangzhou, China, J. Clean. Prod. 231 (2019) 1005–1015, https://doi.org/10.1016/j.jclepro.2019.05.319.

[37] N. Cheng, Research on VOCs Emission Characteristics, Ozone Influencing Mechanism and Pollution Source Tracing in Typical Chemical Industrial Park, Zhejiang University, 2022.

[38] M.A. Elangasinghe, N. Singhal, K.N. Dirks, J.A. Salmond, Development of an ANN–based air pollution forecasting system with explicit knowledge through sensitivity analysis, Atmos. Pollut. Res. 5 (4) (2014) 696–708, https://doi.org/10.5094/apr.2014.079.

[39] M. Gao, L. Yin, J. Ning, Artificial neural network model for ozone concentration estimation and Monte Carlo analysis, Atmos. Environ. 184 (2018) 129–139, https://doi.org/10.1016/j.atmosenv.2018.03.027.

[40] C. Zhang, Y. Song, H. Wang, L. Zeng, M. Hu, K. Lu, S. Xie, W.P.L. Carter, Observation-based estimations of relative ozone impacts by using volatile organic compounds reactivities, Environ. Sci. Technol. Lett. 9 (1) (2021) 10–15, https://doi.org/10.1021/acs.estlett.1c00835.

[41] G. He, T. Deng, D. Wu, C. Wu, X. Huang, Z. Li, C. Yin, Y. Zou, L. Song, S. Ouyang, L. Tao, X. Zhang, Characteristics of boundary layer ozone and its effect on surface ozone concentration in Shenzhen, China: a case study, Sci. Total Environ. 791 (2021), 148044, https://doi.org/10.1016/j.scitotenv.2021.148044.

[42] Z. Tan, X. Ma, K. Lu, M. Jiang, Q. Zou, H. Wang, L. Zeng, Y. Zhang, Direct evidence of local photochemical production driven ozone episode in Beijing: A case study, Sci. Total Environ. 800 (2021), 148868, https://doi.org/10.1016/j.scitotenv.2021.148868.

[43] C. Hu, P. Kang, D.A. Jaffe, C. Li, X. Zhang, K. Wu, M. Zhou, Understanding the impact of meteorology on ozone in 334 cities of China, Atmos. Environ. 248 (2021), 118221, https://doi.org/10.1016/j.atmosenv.2021.118221.

[44] K. Li, L. Chen, F. Ying, S.J. White, C. Jang, X. Wu, X. Gao, S. Hong, J. Shen, M. Azzi, K. Cen, Meteorological and chemical impacts on ozone formation: a case study in Hangzhou, China, Atmos. Res. 196 (2017) 40–52, https://doi.org/10.1016/j.atmosres.2017.06.003.

[45] T. Wang, L. Xue, P. Brimblecombe, Y.F. Lam, L. Li, L. Zhang, Ozone pollution in China: a review of concentrations, meteorological influences, chemical precursors, and effects, Sci. Total Environ. 575 (2017) 1582–1596, https://doi.org/10.1016/j.scitotenv.2016.10.081.
[46] M. Wang, H. Sheng, Y. Liu, G. Wang, H. Huang, L. Fan, D. Ye, Research on the diurnal variation characteristics of ozone formation sensitivity and the impact of ozone pollution control measures in "2 + 26" cities of Henan Province in summer, Sci. Total Environ. 888 (2023), 164121, https://doi.org/10.1016/j.scitotenv.2023.164121.
[47] W.P.L. Carter, Development of a condensed SAPRC-07 chemical mechanism, Atmos. Environ. 44 (40) (2010) 5336–5345, https://doi.org/10.1016/j.atmosenv.2010.01.024.
[48] H. Shen, Z. Sun, Y. Chen, A.G. Russell, Y. Hu, M.T. Odman, Y. Qian, A.T. Archibald, S. Tao, Novel method for ozone isopleth construction and diagnosis for the ozone control strategy of Chinese cities, Environ. Sci. Technol. 55 (23) (2021) 15625–15636, https://doi.org/10.1021/acs.est.1c01567.
[49] H. Fang, W.W. Walters, D. Mase, G. Michalski, i_NRACM: incorporating ^{15}N into the Regional Atmospheric Chemistry Mechanism (RACM) for assessing the role photochemistry plays in controlling the isotopic composition of NOx, NOy, and atmospheric nitrate, Geosci. Model Dev. (GMD) 14 (8) (2021) 5001–5022, https://doi.org/10.5194/gmd-14-5001-2021.
[50] M. Wang, W. Chen, L. Zhang, W. Qin, Y. Zhang, X. Zhang, X. Xie, Ozone pollution characteristics and sensitivity analysis using an observation-based model in Nanjing, Yangtze River Delta Region of China, J. Environ. Sci. (China) 93 (2020) 13–22, https://doi.org/10.1016/j.jes.2020.02.027.
[51] D. Ding, J. Xing, S. Wang, Z. Dong, F. Zhang, S. Liu, J. Hao, Optimization of a NO(x) and VOC cooperative control strategy based on clean air benefits, Environ. Sci. Technol. 56 (2) (2022) 739–749, https://doi.org/10.1021/acs.est.1c04201.
[52] G. Yang, Y. Liu, X. Li, Spatiotemporal distribution of ground-level ozone in China at a city level, Sci. Rep. 10 (1) (2020), https://doi.org/10.1038/s41598-020-64111-3.
[53] N. Afonso, J. Pires, Characterization of surface ozone behavior at different regimes, Appl. Sci. 7 (9) (2017) 944, https://doi.org/10.3390/app7090944.
[54] F.M. Santos, A. Gomez-Losada, J.e.C.M. Pires, Empirical ozone isopleths at urban and suburban sites through evolutionary procedure-based models, J. Hazard Mater. 419 (2021), 126386, https://doi.org/10.1016/j.jhazmat.2021.126386.